Shinji Kohara*, Koji Ohara, Hiroo Tajiri, Chulho Song, Osami Sakata, Takeshi Usuki, Yasuhiko Benino, Akitoshi Mizuno, Atsunobu Masuno, Junpei T. Okada, Takehiko Ishikawa, and Shinya Hosokawa

Synchrotron X-ray Scattering Measurements of Disordered Materials

DOI 10.1515/zpch-2015-0654
Received June 30, 2015; accepted October 8, 2015

Abstract: With the advent of third-generation synchrotron sources and the development of light source techniques, X-ray scattering techniques have become feasible, leading to new approaches for studying the structures of disordered materials in a quantitative manner. We introduce a dedicated diffractometer for high-energy total X-ray scattering measurement and a newly developed anomalous X-ray spectrometer at SPring-8. As advanced methodologies for the measurement of liquids, we now offer three state-of-art levitation instruments for aerodynamic levitation, electrostatic levitation, and acoustic levitation at the SPring-8 beamlines, cover-

***Corresponding author: Shinji Kohara,** Quantum Beam Unit, National Institute for Materials Science (NIMS), Hyogo 679-5148, Japan; and Synchrotron X-ray Station at SPring-8, NIMS, Hyogo 679-5148, Japan; and Information Integrated Materials Research Unit, Research Center For Information Integrated Materials, NIMS, 1-2-1 Sengen, Tsukuba, Ibaraki 305-0047, Japan; and Research & Utilization Division, Japan Synchrotron Radiation Research Institute, Hyogo 679-5198, Japan, e-mail: KOHARA.Shinji@nims.go.jp
Chulho Song: Synchrotron X-ray Station at SPring-8, NIMS, Hyogo 679-5148, Japan
Koji Ohara, Hiroo Tajiri: Research & Utilization Division, Japan Synchrotron Radiation Research Institute, Hyogo 679-5198, Japan
Osami Sakata: Quantum Beam Unit, National Institute for Materials Science (NIMS), Hyogo 679-5148, Japan; and Synchrotron X-ray Station at SPring-8, NIMS, Hyogo 679-5148, Japan
Takeshi Usuki: Graduate School of Science and Engineering, Yamagata University, Yamagata 990-8560, Japan
Yasuhiko Benino: Graduate School of Environmental and Life Science, Okayama University, Okayama 700-8530, Japan
Akitoshi Mizuno: Department of Physics, Gakushuin University, Tokyo 171-8588, Japan
Atsunobu Masuno: Institute of Industrial Science, The University of Tokyo, Tokyo 153-8505, Japan
Junpei T. Okada, Takehiko Ishikawa: Institute of Space and Astronautical Science (ISAS), Japan Aerospace Exploration Agency (JAXA), Ibaraki 305-8505, Japan
Shinya Hosokawa: Department of Physics, Graduate School of Science and Technology, Kumamoto University, Kumamoto 860-8555, Japan

ing a wide temperature range of −40−3000 °C. Furthermore, scientific investigations of glasses, liquids, and amorphous materials reported in the last five years at SPring-8 are reviewed.

Keywords: High-energy X-ray Scattering, Anomalous X-ray Scattering, Glass, Liquid, Amorphous Materials.

1 Introduction

Scattering methods provide average structural information on materials. X-ray and neutron scattering techniques have been widely used to directly measure local and intermediate-range or nanoscale structures, atomic bond lengths, and coordination numbers by Fourier transformation of the total structure factor $S(Q)$ ($Q = (4\pi/\lambda)\sin\theta$, 2θ: scattering angle, λ: photon or neutron wavelength) to a real-space function (pair distribution function, $g(r)$) using the equation

$$g(r) = 1 + \frac{1}{2\pi^2 r\rho}\int_{Q_{\min}}^{Q_{\max}} Q\,[S(Q) - 1]\sin(Qr)\mathrm{d}Q, \tag{1}$$

where ρ is the number density. To obtain real-space information with sufficient resolution, it is necessary to measure $S(Q)$ up to the higher-Q region since a higher resolution in real space is achieved with a larger $Q_{\max}$.

X-ray scattering techniques have become feasible with the arrival of third-generation synchrotron sources and/or the introduction of advanced insertion devices (wigglers and undulators). This is because the use of high-energy ($E >$ 50 keV) X-rays and X-rays near the absorption edge provide us with sufficient resolution in real space and element-specific structure information, respectively. Poulsen et al. [1] reported the first study on silica glass in 1995, which involved pair distribution function (PDF) analysis based on high-energy X-ray total scattering (HEXTS) measurement. They used high-energy X-rays from a wiggler at the HASYLAB, Germany to measure scattering data up to $Q = 30$ Å^{-1}. Since this landmark study, HEXTS measurements have been widely applied to disordered materials from ambient to extreme conditions at the third-generation synchrotron radiation facilities of the European Synchrotron Radiation Facilities (ESRF, France), Advanced Photon Source (APS, USA), and Super Photon ring 8 GeV (SPring-8, Japan). Furthermore, it has become important to apply element-specific scattering techniques to understand the structures of complex disordered materials. The development of the anomalous X-ray scattering (AXS) technique [2] has been recently pursued at ESRF [3, 4], APS [5, 6], and SPring-8 [7]. In this article, we introduce the

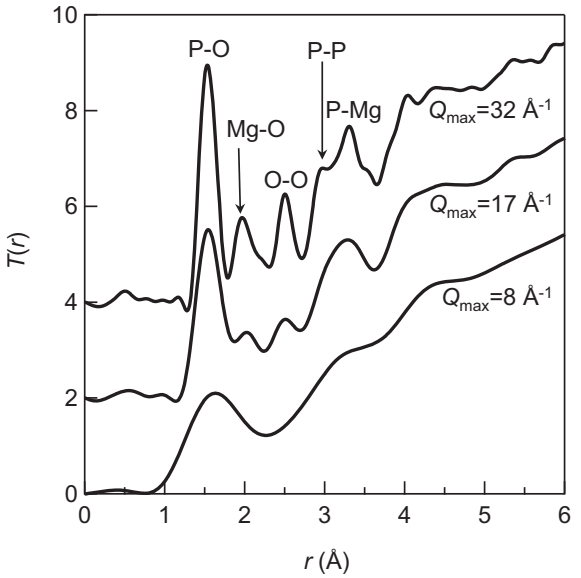

Figure 1: X-ray total correlation functions $T(r)$ for MgP_2O_5 glass obtained by Fourier transformations with different Q_{max}.

instrumentation developed at SPring-8 for the HEXTS and AXS techniques, and for levitation techniques for containerless liquids in a wide temperature range. Furthermore, we review some landmark studies carried out during the last five years.

2 High-energy X-ray total scattering (HEXTS)

The neutron scattering technique has been widely applied to obtain reliable experimental total scattering data since spallation sources allow us to obtain high-Q data with the time-of-flight technique. On the other hand, conventional X-ray sources can provide only low-energy X-rays with an insufficient beam flux, and hence, the maximum obtainable Q is very limited. Figure 1 shows the effect of Q_{max} in the Fourier transformation of $S(Q)$ on the resolution of the total correlation function $T(r)$ (= $4\pi r\rho \cdot g(r)$). It is notable that high-Q data are necessary to study the complex structures of oxide glasses. Scattering experiments using high-energy X-rays have the following advantages:

(i) Although X-ray scattering data typically suffer from a significant decrease in the coherent scattering cross section in the high-Q region owing to the nature of the atomic form factor, high-energy X-rays provide high-Q data with small scattering angles, which can suppress the energy- and 2θ-dependent correction terms (particularly the absorption correction term).

(ii) High-energy X-rays can be used for scattering measurement in the transmission geometry owing to their high penetration power, which allows us to use a millimeter-thickness container for powder and liquid samples containing heavy elements.
(iii) Highly collimated X-rays with sufficient flux make it possible to perform experiments under extreme conditions, including high temperatures and high pressures, because small scattering angles allows the reduction of the window area of the furnace and the high-pressure vessel.

3 Anomalous X-ray scattering (AXS) [2,3,7]

The AXS technique utilizes the anomalous change in the atomic form factor of a specific element that occurs when the energy of incident X-rays is near an absorption edge of the element. The complex atomic form factor of an element is given as

$$f(Q,E) = f_0(Q) + f'(E) + if''(E), \tag{2}$$

where $f_0(Q)$ is the energy-independent term and $f'(E)$ and $f''(E)$ are the real and imaginary parts of the anomalous term, respectively. $f(Q,E)$ is governed by the Q-dependent $f_0(Q)$ in a normal X-ray scattering process, and the anomalous term is negligible. When the energy of incident X-rays approaches an absorption edge of a constituent element, however, $f'(E)$ has a large negative minimum and $f''(E)$ changes abruptly near the corresponding absorption edge energy of each element. One can utilize the difference between two scattering spectra $\Delta_i I(Q)$ near an absorption edge of the ith element, where one signal is typically measured at ~10 eV below the absorption edge, while the other is measured at ~100 eV below the absorption edge (E_{near} and E_{far}, respectively). This differential spectrum is expressed as

$$\alpha_i \Delta_i I(Q, E_{\text{far}}, E_{\text{near}}) = \Delta_i \left[\left\langle f^2 \right\rangle - \left\langle f \right\rangle^2 \right] + \Delta_i \left[\left\langle f \right\rangle^2 \right] \Delta_i S(Q), \tag{3}$$

where α_i is a normalization constant and $\Delta_i[\ ]$ indicates the difference between the values in brackets at the energies of E_{far} and E_{near}, close to the absorption edge of the ith element. The $\Delta_i S(Q)$ functions are given by a linear combination of $S_{ij}(Q)$ as

$$\Delta_i S(Q) = \sum_{i=1}^{N} \sum_{j=1}^{N} w_{ij}(Q, E_{\text{far}}, E_{\text{near}}) S_{ij}(Q), \tag{4}$$

where the weighting factors are given by

$$w_{ij}(Q, E_{\mathrm{far}}, E_{\mathrm{near}}) = x_i x_j \frac{\Delta_i \left[f_i f_j^* \right]}{\Delta_i \left[\langle f \rangle^2 \right]}. \quad (5)$$

It is notable that compared with $S(Q)$, $\Delta_i S(Q)$ enhances the contribution of the ith-element-related partial structure factors and hence suppresses those of other partials.

4 Instrumentations for HEXTS and AXS

4.1 HEXTS diffractometer at BL04B2 of SPring-8

The HEXTS diffractometer [8] dedicated to glass, liquid, and amorphous materials was installed at the high-energy X-ray diffraction beamline BL04B2 [9] of SPring-8 in 1999. The light source at BL04B2 is a bending magnet, which provides horizontally polarized X-rays. The monochromator is a single-bance Si (111) crystal or Si (220) crystal [9]. Photographs of the two-axis diffractometer dedicated to disordered materials and the ancillary equipment are shown in Figure 2. The diffractometer (Figure 2(a)) was designed with a horizontal scattering plane for easier use of heavy equipment, although the scattered X-ray intensity decreases significantly at a large scattering angle in this geometry. In the case of high-energy X-ray scattering, however, experiments can be performed with small scattering angles, at which the effect of the polarization factor is reduced. The diffractometer has two 2θ arms, one is for normal step-scan measurement using three CdTe detectors and the other is for quick measurement using an area detector. The advantage of the step-scan measurement is that it provides high-quality data because the contribution of the background is extremely small owing to the receiving slits and because a CdTe detector can discriminate unfavorable contributions, such as fluorescence from heavy elements. On the other hand, the area detector is useful for quick measurements (for example, an X-ray image intensifier enables scattering data to be measured within a 30 ms shot, Figure 2(b)), although the contribution of the background becomes large and the area detector does not provide sufficient energy discrimination. The advantage of the instrument is that we can switch between the step-scan mode and the quick measurement mode by changing the detector without any other rearrangement of the experimental setup, meaning that we can conveniently perform both measurements depending on the scientific objective. The typical beam size at the sample position is 2.5 mm (H) × 0.5 mm (W), and the size can be further reduced for small samples. For example, one can obtain a reli-

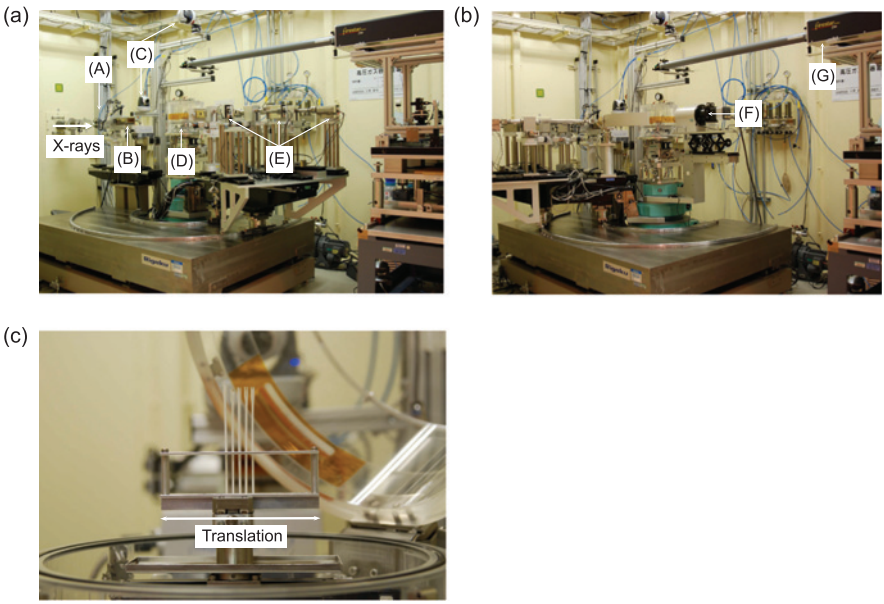

Figure 2: HEXTS diffractometer built at BL04B2 beamline. (A) 4D incident slits, (B) ionization chamber, (C) CCD camera, (D) vacuum chamber (sample), (E) CdTe detectors, (F) X-ray image intensifier, (G) 200 W CO_2 laser

able structure factor in a wide Q-range even with a small amount of sample such 5 mg.

In a typical experiment using the step-scan method at room temperature, an automated sample changer is utilized as the most useful ancillary equipment. The fully automatic sample changer with an x-translation stage (Figure 2(c)) allows automatic measurements to be performed on 14 samples. A conventional high-temperature furnace dedicated to the diffractometer that can reach temperatures of up to 1100 °C is another useful ancillary item. A typical sample container is a Pyrex or silica glass tube of 2 mm inner diameter × 0.15 mm thickness × 65 mm length.

4.2 AXS spectrometer at BL13XU of SPring-8 [7]

The AXS spectrometer was developed at the surface and interface structures beamline BL13XU [10]. The light source of BL13XU is the SPring-8 standard in-vacuum undulator, and a cryogenic Si(111) double-crystal monochromator has been installed [10]. Figure 3 shows the AXS spectrometer attachments in-

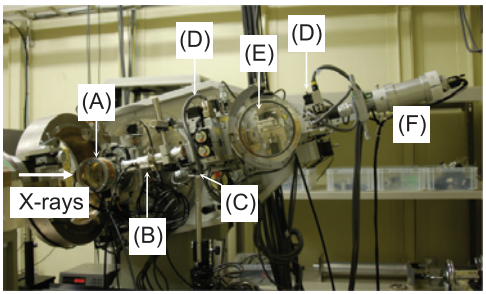

Figure 3: AXS spectrometer attachments installed at BL13XU beamline [7]. (A) vacuum chamber (sample), (B) flight pass, (C) beam stop, (D) slits, (E) LiF analyzer crystal, (F) NaI(Tl) scintillation detector

stalled in the built-in six-circle diffractometer (Kohzu Precision Co. Ltd., TDT-17) at the BL13XU beamline, where the diffractometer operates as a dedicated high-resolution spectrometer by employing a LiF analyzer crystal. The spectrometer mainly consists of the six-circle diffractometer, a vacuum sample chamber, slits, a beam stop, an analyzer crystal, and a NaI(Tl) scintillation detector.

The ideal energy resolution ($\Delta E/E$) of an analyzer crystal is given by

$$\Delta E/E = \Delta\theta/\tan\theta_{\mathrm{B}}, \tag{6}$$

where $\Delta\theta$ and θ_{B} are the rocking-curve width and Bragg angle, respectively. By choosing an analyzer crystal with a sufficient rocking-curve width, the contributions of fluorescence and Compton scattering to an AXS spectrum can be clearly distinguished with sufficient statistics. In addition, it should be pointed out that a LiF crystal is a low-cost product. A vacuum chamber is installed to suppress scattering by air around the sample, which is very important for accurately measuring scattering from disordered materials. The vacuum chamber is also useful for hygroscopic samples. High energy resoluation is an important factor for precise AXS measurements since fluorescence is induced by incident X-rays while measuring near the absorption edge. The energy resolution of the LiF(200) crystal is ca. 12 eV in FWHM at 12 keV, which allows the contributions from fluorescence and Compton scattering to be distinguished. Furthermore, the energy resolution of the LiF(200) crystal is approximately seven times higher than that obtained by sagittal focusing of a cylindrical mosaic graphite crystal [3]. The spectrometer can be used for HEXTS measurement at energies of up to $E \sim 35$ keV without the use of a crystal analyzer, providing us with 100 times higher photon flux than that of the BL04B2 bending magnet beamline.

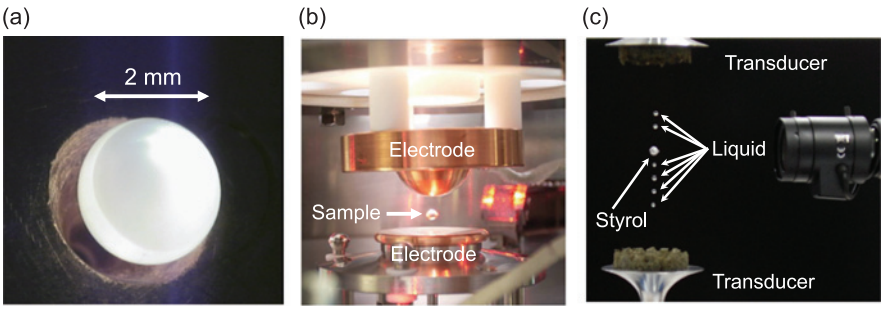

Figure 4: Photographs of aerodynamic levitation (a), electrostatic levitation (b), and acoustic levitation (c) instruments.

5 Levitation techniques

As mentioned in Section 2, the HEXTS technique is feasible under extreme conditions, and hence, relevant levitation techniques have been developed for use with the synchrotron radiation sources [11]. Levitation and containerless methods allow enhanced glass formation owing to the elimination of extrinsic heterogeneous nucleation. They also enable experiments on high-temperature liquids and deeply undercooled liquids without contamination effects from containers. Recently, the use of levitation to study liquids and the formation of glasses from liquids has been of particular interest in understanding the structure of non-glass-forming liquids and the process of glass formation. Three levitation techniques, aerodynamic levitation [11, 12], electrostatic levitation [11, 13, 14], and acoustic levitation [15] are available (Figure 4) at SPring-8.

5.1 Aerodynamic levitation

In the aerodynamic levitation technique [12], a sample is levitated by a gas flow in a convergent-divergent nozzle, where the Bernoulli force pushs the sample back to the axis of the nozzle. Stably levitated samples can then be heated by a continuous wave CO_2 laser. The condition for levitation is derived from the law of momentum conservation applied to a control volume that contains the sample:

$$\int \left[\frac{1}{2}\rho_G \mu^2 + p\right] \mathrm{d}A = Mg, \tag{7}$$

where ρ_G, μ, and p are the gas density, vertical gas flow velocity, and gas pressure, respectively, and Mg is the sample weight. The integral is evaluated over the surface A of the control volume.

5.2 Electrostatic levitation

The electrostatic levitation technique [13] is attractive for the measurement of scattering and thermophysical properties. A charged liquid sample is levitated between a pair of electrodes, and it is free from obstacles, such as the nozzle or coils in other levitators. Moreover, to avoid electrical breakdown when applying a high voltage between the electrodes, electrostatic levitators must be operated under either a pressurized atmosphere (~ 0.4 MPa) or high vacuum. High-vacuum conditions are useful for avoiding the undesiable oxidization of melts.

5.3 Acoustic levitation

Acoustic levitation was recently optimized to levitate low-temperature liquids [15] in a cryojet. This technique has potential for new applications of low-temperature liquids in pharmaceutical [16] and engineering sciences.

A single-axis acoustic levitator [15] can levitate liquid and solid drops of 1–3 mm diameter at temperatures in the range of -40 to $+40\,^{\circ}$C. The levitator comprises two acoustic transducers and an acoustic power supply that controls the acoustic intensity and relative phase of the transducers. The acoustic transducers are operated at their resonant frequency of ~ 22 kHz and can produce sound pressure levels of up to 160 dB. The force applied by the acoustic field can be modulated to excite oscillations in a sample.

6 Applications of HEXTS and AXS

6.1 Silica glass and MCM-41

Silica (SiO_2) glass is the most typical glass-forming material according to Zachariasen [17]. The structure of SiO_2 glass comprises regular SiO_4 tetrahedra sharing oxygen atoms at the corners, yielding a continuous random network. MCM-41 is a prototypical mesoporous material synthesized by researchers at Mobil, and exhibits a regular arrangement of cylindrical mesopores that form a one-dimensional pore system. Figure 5(a) shows the total structure factors $S(Q)$ of

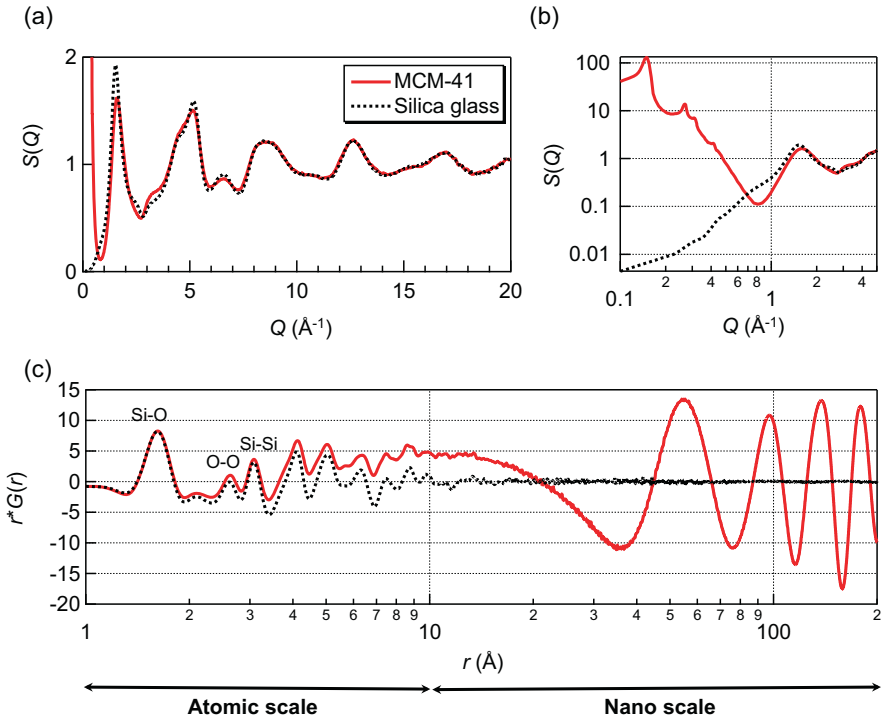

Figure 5: X-ray total scattering data for silica glass and MCM-41. (a) Total structure factor $S(Q)$, (b) enlarged low Q region of $S(Q)$, (c) reduced pair distribution function $G(r)$.

SiO_2 glass and MCM-41 measured at the BL04B2 beamline. The figure shows that $S(Q)$ for silica glass exhibits an first sharp diffraction peak (FSDP) at $Q = 1.55$ Å^{-1}, which is a signature of a continuous random network. $S(Q)$ for MCM-41 is similar to that for SiO_2 glass in the Q range of 1–20 Å^{-1}. However, Bragg peaks can be observed at $Q < 1$ Å^{-1} owing to its hexagonal structure (Figure 5(b)) with a pore size of ~ 55 Å and wall thickness of ~ 10 Å. This feature is clearly visible in the reduced pair distribution function $G(r)(= (g(r) - 1)/4\pi r\rho)$ at the nanoscale shown in Figure 5(c), which is consistent with the neutron PDF data [18].

6.2 AXS measurements of 25BaO-50Nb_2O_5-25P_2O_5 glass

Phosphate glasses have become increasingly important owing to their potential use as novel functional glasses [19, 20] with a low melting point, which can replace multicomponent oxide glasses containing bismuth and lead. However, the

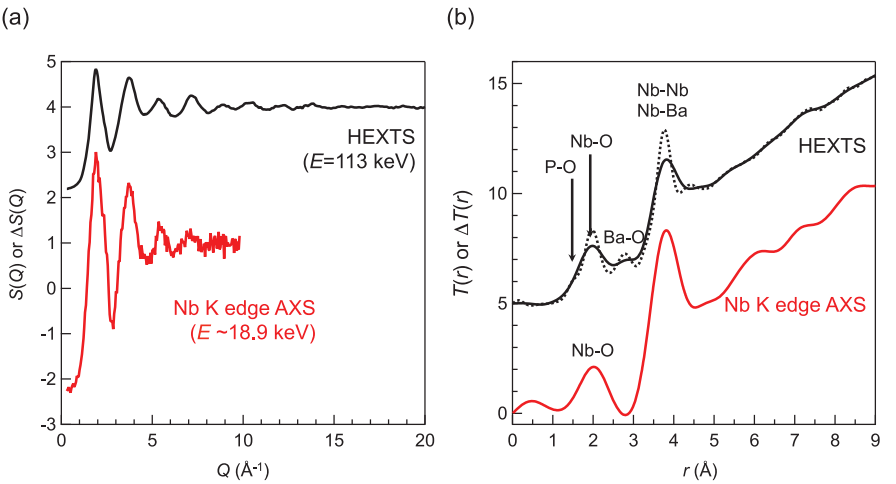

Figure 6: (a) Differential structure factors $\Delta S(Q)$ for Nb in $25BaO\text{-}50Nb_2O_5\text{-}25P_2O_5$ glass together with the total structure factor $S(Q)$ obtained by HEXTS measurement and (b) total correlation functions $T(r)$ for $25BaO\text{-}50Nb_2O_5\text{-}25P_2O_5$ glass. $S(Q)$ and $T(r)$ for HEXTS are displaced upward by 3 and 5 units, respectively, for clarity. The solid and dashed curves of $T(r)$ were obtained by Fourier transformation with $Q_{max} = 9.9$ Å^{-1} and 25 Å^{-1}, respectively [7].

structural analysis of binary and ternary phosphate glasses is difficult owing to their complex nature, although they have been widely studied [21]. The use of AXS can overcome this problem by providing structural information beyond the first coordination distance via element-specific information.

The differential structure factors $\Delta S(Q)$ for Nb in $25BaO\text{-}50Nb_2O_5\text{-}25P_2O_5$ glass together with the total structure factor $S(Q)$ obtained by HEXTS measurement [7] are shown in Figure 6(a). The corresponding total correlation functions $T(r)$ and differential total correlation function $\Delta T(r)$ obtained by Fourier transformation of $\Delta S(Q)$ are shown in Figure 6(b). The contrast between the HEXTS data (black) and Nb K edge AXS data is distinct. Although the resolution in the real space is different between the two data sets, owing to the different Q_{max}, it is demonstrated that the Ba-O correlation is eliminated in the AXS data. Furthermore, significant oscillations are observed between 6 and 9 Å in the AXS data, suggesting that niobium atoms exhibit specific ordering beyond the first coordination distance.

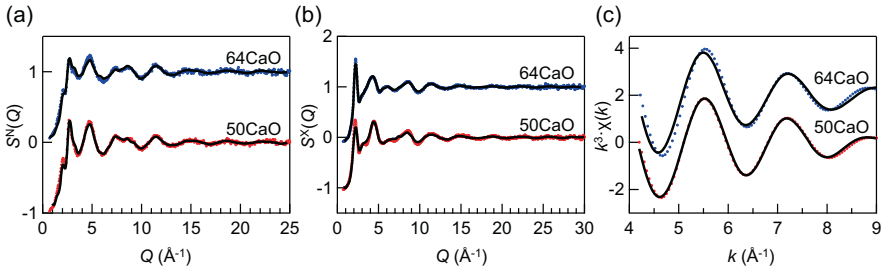

Figure 7: Neutron (a) and X-ray (b) total structure factors $S(Q)$ and EXAFS $k^3 \cdot \chi(k)$ (c) data for 50CaO glass and 64CaO glass. The EXAFS $k^3 \cdot \chi(k)$ data were obtained by back Fourier transformation of the first correlation peak in |FT|. Circles, experimental data; curve, DFT–RMC model [23].

6.3 Atomic and electronic structures in CaO-Al_2O_3 glass

Understanding the atomic structure and bonding upon glass formation is one of the most important scientific topics in glass science. The reverse Monte Carlo (RMC) modelling technique [22] was recently combined with density functional theory (DFT) to reveal the relationship between the atomic/electronic structure and glass-forming ability in several oxide glasses. The general advantage of this combination is that the RMC method can produce large atomic configurations that are consistent with measured scattering and extended X-ray absorption fine structure (EXAFS) data, while the DFT calculations can optimize the RMC configurations to provide information about the energetics and electronic structure.

Levitation techniques allow us to prepare high purity samples of 64CaO-36Al_2O_3 (high glass-forming ability (GFA)) and 50CaO-50Al_2O_3 (low GFA) glasses, because nucleation events can be suppressed owing to the lack of a heterointerface. A glass bead of 2 mm diameter can be obtained by interrupting the laser heating of a containerless levitated liquid, providing a cooling rate of approximately 1000 K/s.

Figures 7a–c show the experimental neutron and X-ray total structure factors $S^{N,X}(Q)$ and the EXAFS $k^3 \cdot \chi(k)$ data, respectively, of 50CaO-50Al_2O_3 (50CaO) glass and 64CaO-36Al_2O_3 (64CaO) glass as colored dots, toghether with the results of DFT–RMC simulation as black curves. The difference between both the scattering and the EXAFS data is small for the two compositions, implying that the short-range structure is similar in the compositions.

The partial pair distribution functions $g_{ij}(r)$ of the above CaO-Al_2O_3 glasses obtained by DFT–RMC simulation are shown in Figure 8. The large-scale atomic configurations of 1078 atoms provided sufficient statistics in real space. Both the

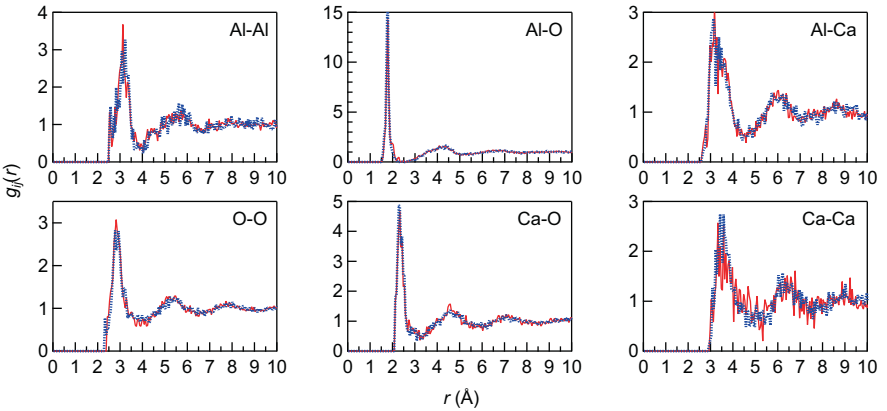

Figure 8: Partial pair distribution functions $g_{ij}(r)$ for the 50CaO and 64CaO glasses obtained by DFT–RMC simulation [23].

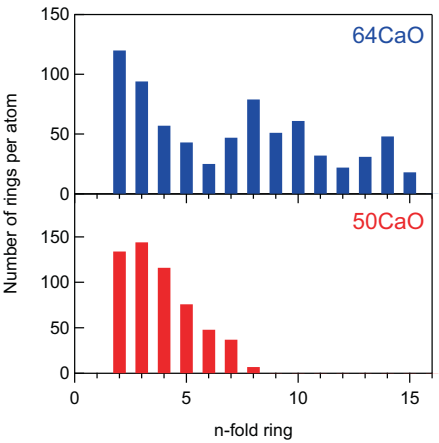

Figure 9: Distribution of –Al(Ca)–O–Al(Ca)–O–Al(Ca)– rings in 50CaO and 64CaO glasses obtained by DFT–RMC simulation [23].

first Al-O and Ca-O correlation peaks are well-defined and sharp owing to the formation of Al-O and Ca-O bonds, respectively. Note that the difference between the 50CaO glass and 64CaO glass is very small, suggesting that their atomic correlations are very similar. Indeed, the Al-O coordination number $N_{\mathrm{Al-O}}$ calculated up to 2.5 Å is 4.26 for the 50CaO glass and 4.14 for the 64CaO glass, and $N_{\mathrm{Ca-O}}$ calculated up to 2.8 Å is 5.02 for the 50CaO glass and 4.92 for the 64CaO glass. These results suggest that AlO_4, AlO_5, AlO_6, CaO_4, CaO_5, and CaO_6 polyhedra are the predominant short-range structural units in the CaO-Al_2O_3 glasses.

Figure 9 shows the distribution of –Al(Ca)–O–Al(Ca)–O–Al(Ca)– rings in the CaO-Al_2O_3 glasses. The 64CaO glass (high GFA) has a wide ring size distri-

bution, while the 50CaO glass (low GFA) has a very narrow ring size distribution. This trend can be understood in terms of the concept of topological order–disorder according to Gupta and Cooper [24]. We also found similar behavior in a MgO-SiO_2 glass with a silica-rich composition [25], which exhibited topological disorder (many large rings with a wide ring size distribution) and higher GFA than that of silica-poor glass.

This characteristic ring size distribution, and particularly the formation of large rings, indicates the existence of a crucial intermediate-range structure at the eutectic composition of 64CaO glass, which exhibits high viscosity in an undercooled liquid, yielding high GFA. Furthermore, it is suggested that the topological disorder in the 64CaO glass is a signature of a "stronger" liquid [26] than that of the 50CaO composition. This scenario can reasonably explain the high GFA of the 64CaO glass without the need for the presence of a traditional network former, as proposed in Zachariasen's original theory [17]. Moreover, this characteristic atomic structure in the 64CaO glass can be understood on the basis of the "cage structure" model proposed by Kim et al. [27].

Recently, C12A7:e-electride glass has been synthesized from a strongly reduced high-temperature melt by Kim et al. [27]. It is assumed that the removal of excess O atoms from AlO_5 and AlO_6 units in the C12A7 melt results in the formation of more extended cage structures in the electride version of the glass, which can host solvated electrons. To shed light on the formation of the electride glass, the highest occupied molecular orbital (HOMO) and lowest unoccupied molecular orbital (LUMO) single-particle states of electrons were computed for the 64CaO glass by DFT as illustrated in Figures 10(a) and (b). The characters of the HOMO and LUMO states are considerably different: while the former is located across atoms and bonds (Figure 10(a)), the latter is associated with a cavity (cage), forming a spin-paired state analogous to an F-center in a vacancy site of crystalline MgO (h_1 in Figure 10(b)). The computed HOMO–LUMO gap is 1.71 eV. Since it is well known that DFT calculations at this level underestimate band gaps by approximately a factor of two, this value is consistent with the typical insulating electronic behavior and transparent properties of the glass. Furthermore, our DFT–RMC model suggests that the first three cage-trapped LUMO states appear as impurity states below the onset of the conduction band. Following the idea of bipolaron states and conducting electride glass, we removed one oxygen atom from the h_2 site in Figure 10(b), thus releasing two additional electrons from the Al/Ca cations in the system while keeping the total charge neutral, and then the structure was optimized for several spin configurations by DFT. In the spin-degenerate case, where there is no distinction concerning the "spin" of electrons, these electrons occupy a cavity vacated by the removed oxygen (marked as h_2), yielding a HOMO state similar to that of the LUMO state of the parent system. On

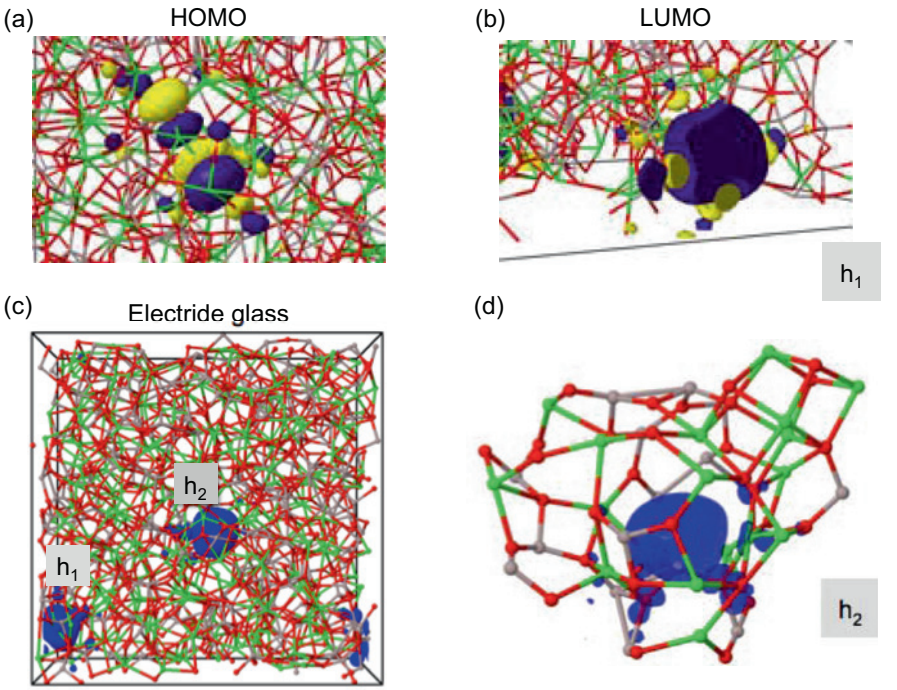

Figure 10: Close-up visualizations of (a) HOMO and (b) LUMO single-particle electron states in the 64CaO glass. h_1 indicates the cavity (cage) occupied by the LUMO. Yellow and magenta represent for different signs of the wave-function nodes. (c) Simulation box and the electron spin density of the 64CaO glass with one oxygen removed at h_2, i.e., with two additional electrons. (d) Cage structure around the spin density of one electron corresponding to the h_2 cavity (close-up of (c)). Al, gray; Ca, green; O, red [23].

the other hand, the removal of the spin-degeneracy (triplet spin configuration) leads to a 0.97 eV more energetically favorable electronic configuration, where the two additional electrons have the same spin and are located in well-separated cavities (Figure 10(c), h_1 and h_2). This procedure was repeated for two, three, and four removed oxygen atoms (four, six, and eight additional electrons), and in all cases, the separated (solvated) electrons in individual cages were energetically more favorable than the F-center-like states (two electrons in one cavity). An example of the cage structure around a single electron (spin density) is presented in Figure 10(d). These cases confirm that by removing oxygen from the standard stoichiometry, one can achieve local spin states in the 64CaO glass. Furthermore, the gradual removal of O increases the number of impurity states within the elec-

tronic band gap, which leads to changes in conductivity due to a narrower band gap.

6.4 Fast-phase-change materials

Although data storage on a DVD is part of our digital world, the physical basis of the storage mechanism is not understood in detail. Information is stored on a DVD in the form of microscopic bits in a thin layer of a polycrystalline alloy containing several elements. The bits can have a disordered, amorphous or an ordered, crystalline structure. The transition between the two phases lasts only tens of nanoseconds and can be triggered by a laser pulse [28]. The combination of synchrotron radiation HEXTS and AXS measurements and RMC/density function theory (DF)–molecular dynamics (MD) simulations has enabled the structures of both phases to be determined for the first time and allowed the establishment of a model to explain the rapid phase change and its high durability [29].

Figure 11(a) shows the X-ray total scattering structure factors $S(Q)$ for crystalline (*c*-) GST and amorphous (*a*-) GST. $S(Q)$ for *c*-GST exhibits sharp Bragg peaks and a diffuse scattering pattern, while only the latter appears for *a*-GST. It was demonstrated that $S(Q)$ for the RMC model (solid curve) is in good agreement with experimental data (open circles). The differential structure factors $\Delta S(Q)$ for Sb and Te obtained from AXS measurements are shown in Figure 11(b). As can be seen in the figure, there are substantial differences between the Sb- and Te-related data at $Q < 6\ \text{Å}^{-1}$, indicating that AXS measurements can be used to distinguish Sb (atomic number of 51)-related correlation and Te (atomic number of 52)-related correlation beyond the nearest neighbor distance.

The coordination numbers in *a*-GST were calculated up to 3.2 Å using the RMC/DF–MD model. In *c*-GST, both Ge and Sb are sixfold coordinated while the total coordination number of Te is 4.8 owing to a vacancy at the Ge/Sb mixing site. These results are in good agreement with the average structure of rocksalt, implying that disorder in the crystalline phase does not have any effect on the average coordination number. Baker et al. reported on the basis of EXAFS measurements [30] that both Ge and Sb obey the so-called 8-N rule and that Te is overcoordinated in *a*-GST, while Akola et al. reported that Sb and Te are overcoordinated on the basis of atomic configurations obtained by RMC/DF–MD simulation using only HEXTS data [31]. In our RMC model refined by employing AXS data, the total coordination numbers for Ge, Sb, and Te are 3.8, 3.1, and 2.5, respectively. Antimony has a lower coordination number than that in the previous RMC/DF–MD model ($N_{Sb} = 3.3$ in Reference [31]). As a result, now both Ge and Sb obey the 8-N rule and only Te is overcoordinated. These results are in line with the

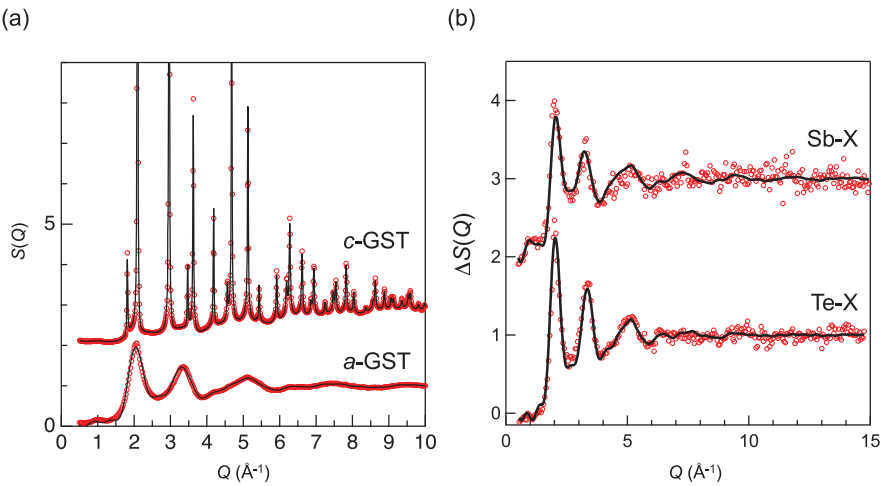

Figure 11: Comparison between the experimental structure factors (open circles) and the results of RMC modelling (solid curve). (a) X-ray total structure factors $S(Q)$ for c-GST and a-GST obtained by HEXTS measurements. (b) $\Delta S(Q)$ for a-GST obtained by AXS measurements at Sb and Te K absorption edges. $S(Q)$ of c-GST and $\Delta S(Q)$ for Sb are displaced upward by 2 units for clarity [29].

results of EXAFS measurements [30] and with Olson et al.'s argument, in which they mentioned the possibility of overcoordinated Te if there are no homopolar (Ge-Ge, Sb-Sb, Te-Te) bonds in a-GST [32].

As the simplest tool for analyzing correlations beyond the pair correlation, the bond angle distributions of Te-Ge-Te and Te-Sb-Te triplets in c-GST and a-GST were calculated. The distributions of Te-Ge-Te and Te-Sb-Te triplets in c-GST exhibit peaks at 90° and 180° owing to its rocksalt structure. The bond angle distributions in a-GST show a similar trend, but the peak widths are larger and the magnitude of the peak at 180° is significantly smaller. Note that the magnitude of the peak at 90° for a-GST is comparable to that for c-GST, although the bond angle is somewhat larger in a-GST, particularly for Te-Ge-Te triplets, owing to the small contribution from tetrahedral Ge. This feature is consistent with the results of an *ab initio* MD simulation reported by Caravati et al. [33]. Kim et al. mentioned the occurrence of threefold p-like bonding in a-GST [34] on the basis of hard X-ray photoemission spectroscopy data, which is consistent with the peaks at 90° and 180° in the bond angle distributions of our revised RMC model.

To obtain statistical structural features beyond the nearest coordination distance, ring statistics were calculated by shortest-path analysis [35]. As can be seen in Figure 12(a), fourfold and sixfold rings consisting of –Ge(Sb)–Te– units are dominant in c-GST. The existence of sixfold rings is due to the 20% vacancy rate

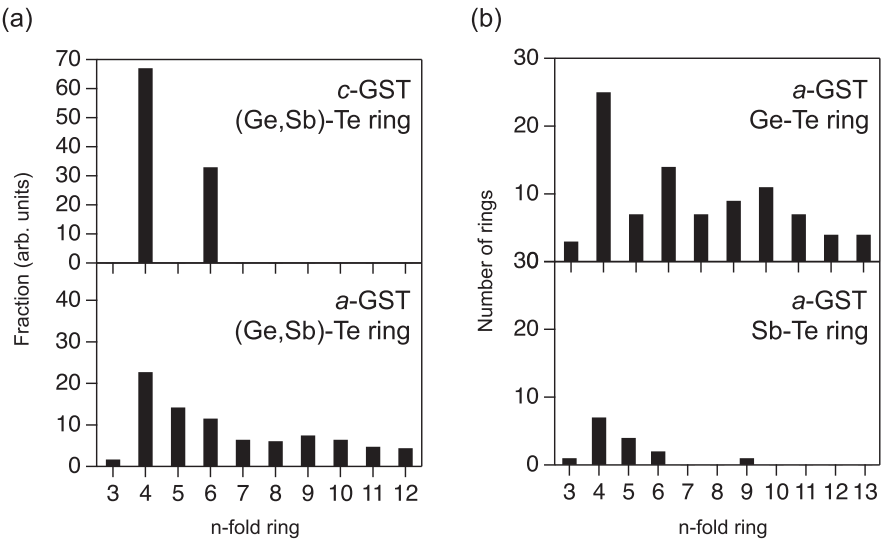

Figure 12: Ring statistics for *c*-GST and *a*-GST obtained from RMC models. (a) Normalized fraction of –Ge(Sb)–Te– rings. (b) Numbers of –Ge–Te– rings and –Sb–Te– rings in *a*-GST. The total number of –Ge(Sb)–Te– rings is normalized because the number of particles in the simulation box is not the same for *c*-GST and *a*-GST. The numbers of –Ge–Te– rings and –Sb–Te– rings clearly show that –Ge–Te– rings form a covalent network and that the –Sb–Te– rings do not contribute to this network in *a*-GST [29].

at Ge/Sb mixing sites. As discussed in Reference [31], small –Ge(Sb)–Te– rings such as fourfold, fivefold, and sixfold rings are dominant in *a*-GST. The numbers of rings consisting of –Ge–Te– units and of –Sb–Te– units in *a*-GST are shown in Figure 12(b). Our RMC model refined by the introduction of AXS data demonstrates that the large fractions of fourfold and sixfold rings are mainly formed by Ge-Te bonds. Therefore, it is suggested that the core network constructed from Ge-Te covalent bonds in *a*-GST is similar to that in *c*-GST, and that this core network plays an important role in ensuring long-term stability of the amorphous phase at room temperature.

To reveal the atomic ordering by Ge-Te and Sb-Te bonds in detail, the connectivities of atoms were calculated for various maximum distances (r_{max}) within which atomic pairs were considered to be connected. As can be seen in Figure 13(a), about 60% of the Ge-Te bonds form a continuous core network when r_{max} is 3.2 Å, whereas Sb-Te bonds do not form such a network when r_{max} is 3.2 Å. This distance corresponds to the covalent bond length determined by DF–MD simulation [36], and both Ge and Sb satisfy the 8-N rule at 3.2 Å in our refined RMC model (N_{Ge} = 3.8 and N_{Sb} = 3.1). The atomic configurations of Ge-Te and Sb-

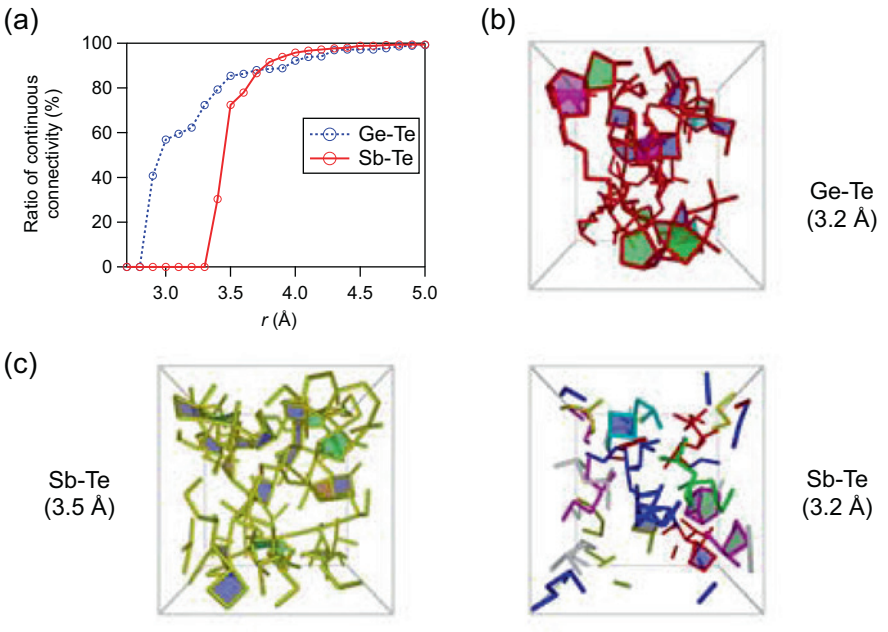

Figure 13: Atomic configuration and connectivity of Ge-Te and Sb-Te in *a*-GST obtained by the RMC model. (a) Connectivity of Ge-Te and Sb-Te for different values of r_{max}. (b) Atomic configuration of Ge-Te and Sb-Te (connectivity of Ge-Te and Sb-Te for $r_{max} = 3.2$ Å). (c) Atomic configuration of Sb-Te (connectivity of Sb-Te for $r_{max} = 3.5$ Å) [29].

Te with bonds considered up to a distance of 3.2 Å are shown in Figure 13(b). It can be clearly observed that Ge-Te bonds form a core network, which stabilizes the amorphous phase, whereas Sb-Te bonds do not. Furthermore, it is evident that Ge-Te bonds form large fractions of fourfold (highlighted in blue) and sixfold (highlighted in light blue) rings. On the other hand, about 70% of the Sb-Te pairs form a pseudonetwork, as can be seen in Figures 13(a) and (c), when when r_{max} is 3.5 Å (in this case, the coordination numbers of Te around Ge ($N_{Ge\text{-}Te}$) and Sb ($N_{Sb\text{-}Te}$) are 4.1 and 3.1, respectively). In other words, the Sb-Te pseudonetwork becomes visible when we increase the correlation distance to 3.5 Å, while such a feature cannot be observed for Ge-Te connectivity.

On the basis of the structural features in *a*-GST found above, we illustrate the phase-change scheme in Figure 14. As highlighted in red in Figure 14, Ge-Te bonds significantly contribute to the network comprising by fourfold rings. Therefore, Ge and Te can be recognized as network-forming elements that ensure the long-term stability of the amorphous phase at room temperature, although amorphous (*a*-) GeTe is not a network former. The core Ge-Te network may remain in the crys-

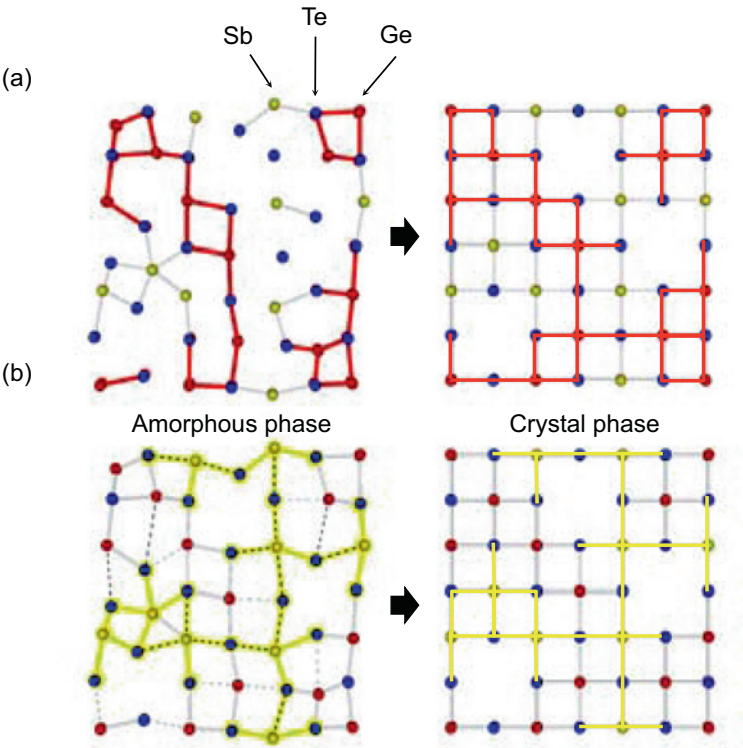

Figure 14: Schematic drawing of phase-change process in *a*-GST where (a) highlights the Ge-Te core network and (b) highlights the Sb-Te pseudonetwork. The sticks represent Ge-Te and Sb-Te bonds up to 3.2 Å and the dotted lines show Sb-Te correlations of 3.2 to 3.5 Å in the amorphous phase [29].

talline phase, which explains the rapid crystallization. As highlighted in yellow in Figure 14(b), the Sb-Te correlations beyond the nearest coordination distance form a Sb-Te pseudonetwork. This unusual atomic ordering in terms of Sb-Te correlations can be ascribed to the combination of two positively charged atoms (Ge, – 0.22 electrons; Sb, 0.32 electrons; Te, 0.22 electrons [36]) and allows the amorphous phase to form critical nuclei via the formation of Sb-Te bonds by small atomic displacements of antimony and tellurium atoms. Thus, our finding can reasonably explain why the crystallization of *a*-GeTe is very rapid in PC-RAM [37] and why the crystallization of *a*-GST is faster than that of *a*-GeTe in DVDs [38].

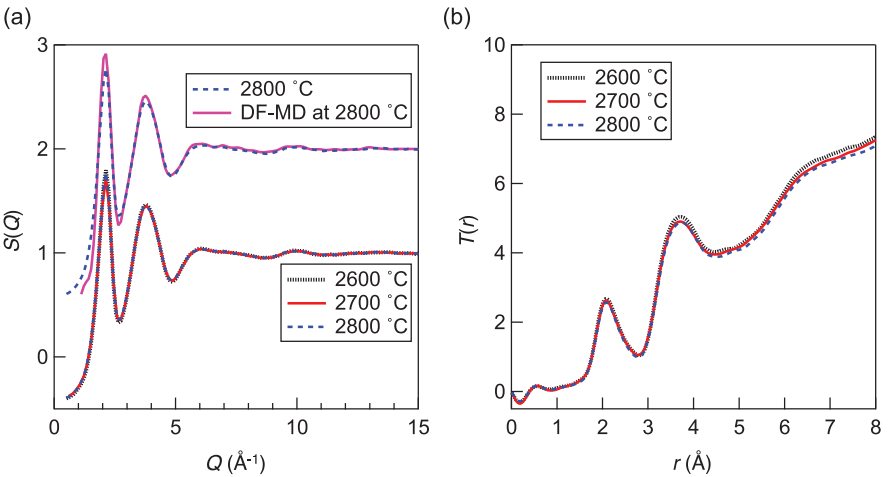

Figure 15: (a) Faber–Ziman total structure factors $S(Q)$ for l-ZrO_2 at 2600–2800 ˚C together with $S(Q)$ derived from a DF–MD simulation at 2800 ˚C. Both the experimental and DF–MD simulation data at 2800 ˚C are displaced upward by 1 unit for clarity. (b) Total correlation functions $T(r)$ for l-ZrO_2 at 2600–2800 ˚C [41].

6.5 High-temperature levitated liquids

The use of levitation techniques has recently uncovered the structures of the high-temperature oxide melts Al_2O_3 [39], Y_2O_3 [40], Ho_2O_3 [40], La_2O_3 [40], ZrO_2 [40, 41], and UO_2 [42] using the high quality data together with simulation techniques.

Figure 15(a) shows the Faber–Ziman [43] X-ray total structure factors $S(Q)$ for liquid (l-) ZrO_2 at 2600–2800 ˚C. The structural change between the liquid at 2800 ˚C and the undercooled liquid at 2600 ˚C is small. A sharp peak is observed at $Q = 2$ Å^{-1}. The X-ray total correlation functions $T(r)$ for l-ZrO_2 (Figure 15(b)) also show small differences in the real space. The first correlation peak observed at about 2.1 Å is assigned to Zr-O correlation and the significant tail to ~ 3 Å implies the formation of asymmetrical ZrO_n polyhedra in the liquid. The second peak observed at about 3.7 Å can be assigned mainly to Zr-Zr correlation, and the contribution of O-O correlation is unclear owing to its small weighting factor for X-rays. The Zr-O correlation length of 2.1 Å is significantly longer than those of Si-O (~ 1.63 Å [44] at 1600–2100 ˚C) and Al-O (~ 1.78 Å [39] at 2127 ˚C) owing to substantial differences between the ionic radii of silicon, aluminum, and zirconium ions [45]. The increased cation-oxygen correlation length in l-ZrO_2 suggests that the oxygen coordination number around zirconium is higher than four because 2.1 Å is close to the sum of the ionic radii of oxygen (1.35 Å [45]) and sixfold

zirconium (0.72 Å [45]). The intermediate-range structure of l-ZrO_2 is therefore made up of large, interconnected polyhedral units and is very different from those of l-SiO_2 and l-Al_2O_3. This suggests that the peak observed at $Q = 2$ Å^{-1} in $S(Q)$ in Figure 15(a) is not the FSDP, which is typically associated with intermediate-range ordering in disordered materials, meaning that there is no such ordering in l-ZrO_2.

The total structure factor $S(Q)$ obtained from the DF–MD simulation at 2800 °C is shown in Figure 15(a) as a solid magenta curve. The agreement with the experimental data is excellent. Additional insight into the intermediate-range ordering of l-ZrO_2, in comparison with that of l-SiO_2 and l-Al_2O_3, can be found by calculating the Bhatia–Thornton [46] number-number partial structure factor $S_{NN}(Q)$,

$$S_{NN}(Q) = c_A^2 S_{AA}(Q) + 2c_A c_B S_{AA}(Q) S_{BB}(Q) + c_B^2 S_{BB}(Q) \quad (8)$$

where $S_{ij}(Q)$ is a Faber–Ziman partial structure factor and c_i denotes the atomic fraction of chemical species i [47]. Figure 16(a) shows $S_{NN}(Q)$ for l-ZrO_2 at 2800 °C compared with those for l-Al_2O_3 at 2127 °C [39] and l-SiO_2 at 2100 °C [44]. Only l-SiO_2 exhibits an FSDP at $Qr_{AX} = 2.7$ (r_{AX} is the atomic cation (A) – anion (X) distance in AX polyhedra). Neither l-Al_2O_3 nor l-ZrO_2 shows an FSDP in $S_{NN}(Q)$, although a small contribution arising from Zr-O and O-O correlations can be observed at $Qr_{AX} = 2.2$ in the l-ZrO_2 data. Since the Bhatia–Thornton $S_{NN}(Q)$ can eliminate the weighting factors for X-rays, the absence of an FSDP in $S_{NN}(Q)$ for l-ZrO_2 is a signature of a non-glass-forming liquid.

The coordination number distributions of l-SiO_2 [44], l-Al_2O_3 [40], and l-ZrO_2 calculated from the structural models are shown in Figure 16(b). SiO_4 tetrahedra are predominant in l-SiO_2 [44], while l-Al_2O_3 comprises AlO_3, AlO_5, and AlO_6 units as well as fourfold Al. For l-ZrO_2, the most common configurations are ZrO_5, ZrO_6, and ZrO_7. Although ZrO_2 and Al_2O_3 have different stoichiometries, this comparison supports our view that the variety of oxygen coordination around cations in l-ZrO_2 is another characteristic feature of non-glass-forming behaviour, because it can disturb the evolution of intermediate-range ordering.

To obtain structural features beyond the first coordination distance, a polyhedral connection analysis was performed for l-SiO_2 [44], l-Al_2O_3 [40], and l-ZrO_2. Figure 16(c) shows the fractions of corner-sharing, edge-sharing, and face-sharing polyhedral units in the liquids. The corner sharing of oxygen is prevalent in l-SiO_2 [44], which is a unique feature of glass forming liquids (GFLs) according to Zachariasen [17]. However, both l-Al_2O_3 and l-ZrO_2 exhibit a considerable amout of oxygen edge sharing, implying that the variety of polyhedral connections is

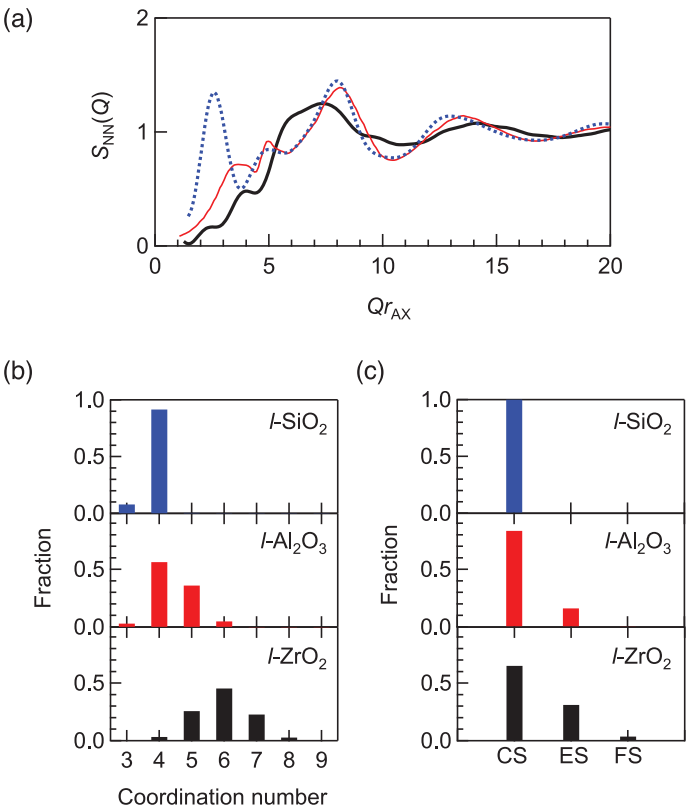

Figure 16: (a) Bhatia–Thornton number-number partial structure factor $S_{NN}(Q)$ for l-ZrO_2 at 2800 °C derived from the DF–MD simulation (bold curve) [41] in comparison with those for l-Al_2O_3 at 2127 °C (solid curve) [40] and l-SiO_2 at 2100 °C (dotted curve) [44]. The momentum transfer Q was scaled by r_{AX}, which r_{AX} is the first coordination distance between A and X in the real-space function. (b) Coordination number distribution of oxygen around the cations in l-ZrO_2 at 2800 °C, l-Al_2O_3 at 2127 °C [40], and l-SiO_2 at 2100 °C [44]. (c) Polyhedral connections in l-ZrO_2 at 2800 °C, l-Al_2O_3 at 2127 °C [40], and l-SiO_2 at 2100 °C [44]. CS, corner-sharing of oxygen; ES, edge-sharing of oxygen; FS, face-sharing of oxygen.

a further characteristic feature of single component non-glass-forming oxide liquids.

Electronic structure analysis was carried out in terms of the electronic density of states (DOS), Wannier functions (WFs), and effective charges for snapshots of the high-temperature phases of crystalline (c-) ZrO_2 and l-ZrO_2. The DOS (above – 20 eV) of c- and l-ZrO_2 and its projections (P-DOS) for l-ZrO_2 are shown in Figure 17(a). The P-DOS plots reveal that this part of the electronic spectrum is mainly associated with oxygen (O-2p orbitals) and that the Zr semicore

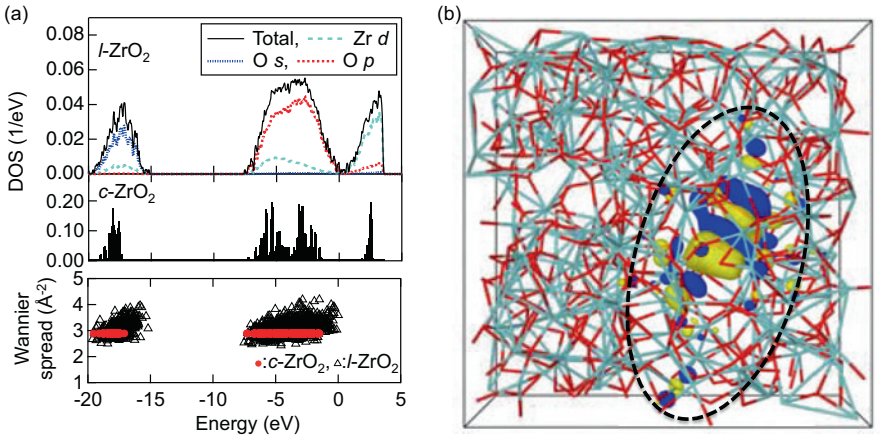

Figure 17: (a) DOS and its projections onto atomic orbitals for the higher valence bands and conduction band, together with the Wannier function spreads (occupied states).
(b) Visualization of the HOMO state (KS orbital) in l-ZrO_2. Yellow and blue isosurfaces denote different signs of the wavefunction nodes [41].

states corresponding to the atomic Zr-4s and Zr-4p orbitals are deeper (below – 20 eV, not shown). The zirconium d-component dominates in the conduction band of l-ZrO_2. The effect of a high temperature on the distorted ZrO_n polyhedra in l-ZrO_2 is evident as a broadening of the energy bands, and the gap between the valence and conduction bands disappears (the calculated band gap is 3.26 eV for c-ZrO_2).

The difference between the electronegativities of Zr (1.3) and O (3.5) indicates that the chemical bonding between the two elements is mainly ionic, and this is supported by the significant weight of the oxygen P-DOS for the highest valence band. The effective charges calculated by the Bader method [48] are +2.62e and −1.31e for Zr and O in l-ZrO_2, respectively, and reflect the ionic bonding. The atomic charges in l-ZrO_2 are very similar to those in the crystalline phase, which is in accordance with our previous studies on CaO-Al_2O_3 [23] and MgO-SiO_2 glasses [25]. The associated atomic volumes imply that the increased oxygen volume in l-ZrO_2 compensates for the decreased oxygen coordination, and this results in comparable atomic charges for the two phases. Similar behavior has been found for MgO-SiO_2 glass [25].

The maximally localized WF can be considered as a natural generalization of localized molecular orbitals in solids, and they provide valuable insight into chemical bonding. The WFs have been obtained from the occupied Kohn-Sham (KS) orbitals by a unitary transformation, where the spatial extension (spread) of the WF orbitals is minimized. For each WF orbital, the center of the WF indicates

the most probable point for locating an electron (or an electron pair in the case of a spin-degenerate orbital), and the corresponding Wannier spread is a direct measure of the degree of localization. The distribution of Wannier spreads is shown in Figure 17(a). The oxygen coordination is smaller ($N_{OZr} \sim 3$) and less regular in the liquid than in the crystal. There is considerable scatter in the spreads and the WFs are considerably less localized than the crystal which has a value of ~ 2.9.

The HOMO is also visualized in Figure 17(c), where the KS orbital (HOMO) is delocalized over a group of atoms highlighted by a dashed circle, while the transformed WFs for the HOMO and HOMO-1 (molecular orbitals) are each localized over one Zr-O bond [41]. The WF shapes in these examples are very similar to those in the high-temperature phase of c-ZrO_2 but there are also cases with considerable deviation, as can be expected from the scatter of WF spreads (Figure 17(a)).

The origin of the FSDP associated with the formation of intermediate-range ordering in oxide glasses and liquids remains controversial, because the inherent disorder complicates the ability of AX polyhedral connections to form an A-X network. SiO_2 has exceptionally high GFA, and the origin of the FSDP in SiO_2 has often been studied. The results are summarized in Reference [49]. The random network model of Zachariasen [17], which was modified for an oxide glass in References [50] and [51] (illustrated in Figure 7 of Reference [49]), demonstrates that the intermediate-range ordering arises from the periodicity of boundaries between successive small cages in the network formed by connected, regular SiO_4 tetrahedra with shared oxygen atoms at the corners. It has also been suggested that the small cages are topologically disordered [24], resulting in a broad distribution of ring sizes from threefold to twelvefold rings centered at sixfold rings [25]. This is reflected in $S_{NN}(Q)$ for l-SiO_2 (Figure 16(a)), where the FSDP width is broader than that of the corresponding Bragg peak in the crystalline phase (β-cristobalite, c-SiO_2), where only a sixfold ring contributes. Figure 18(a) and (b) shows three-dimensional atomic configurations and schematic illustrations of c-SiO_2 and l-SiO_2, respectively. The crystalline phase exhibits only sixfold rings of six SiO_4 tetrahedra, resulting in long-range periodicity (dashed cyan lines in Figure 18(a)). However, some pseudo Bragg planes (dashed cyan lines in the left panel of Figure 18(b)) can be recognized in l-SiO_2. Although the introduction of different ring sizes can easily modify the crystalline topological order (Figure 18(b)), the interconnection of regular SiO_4 tetrahedra with shared oxygen at corners only yields the broadened Bragg peak as the FSDP.

As can be seen in Figure 16(a), an FSDP is absent in $S_{NN}(Q)$ for l-ZrO_2. This is because the variety of short-range structural units with large oxygen coordination, ZrO_5, ZrO_6, and ZrO_7, and the large contribution of oxygen edge sharing prevent the formation of intermediate-range ordering. A similar feature can be expected in

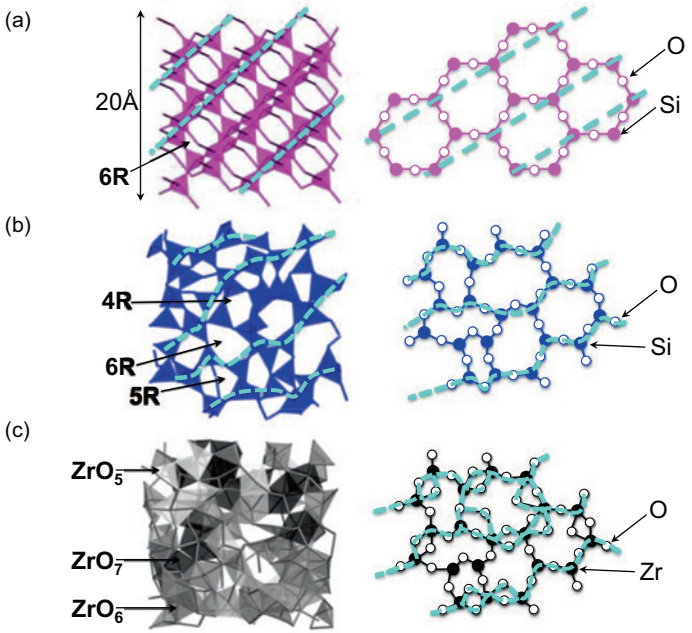

Figure 18: Atomic configurations and schematic illustrations of (a) c-SiO_2, (b) l-SiO_2, and (c) l-ZrO_2. The periodicity of the cage boundaries is highlighted by dashed lines and curves [41].

l-Y_2O_3 and l-La_2O_3 because their Faber–Ziman partial structure factors $S_{ij}(Q)$ do not contribute to the expected Q position of ~ 1 $Å^{-1}$ for an FSDP [40]. Short-range structural disordering in l-ZrO_2 is further demonstrated in the three-dimensional atomic configuration and the schematic illustration of l-ZrO_2 (Figure 18(c)). The periodicity of boundaries (dashed lines) is suppressed by edge sharing of oxygen associated with the formation of ZrO_5, ZrO_6, and ZrO_7. Although ZrO_2 forms a network structure by interconnecting AX polyhedra in the liquid phase, we have shown that the various short-range structural units and their connectivity cause disorder at the intermediate range and prevent the evolution of an FSDP for the liquid. Our results demonstrate that the absence of an FSDP in $S_{NN}(Q)$ can be an important indicator of single component non-glass-forming oxide liquids, but this does not necessarily apply similarly to other non-GFLs.

The absence of an FSDP in $S_{NN}(Q)$ suggests that both l-Al_2O_3 and l-ZrO_2 are very fragile liquids [26]. This suggestion is supported by a comparison with l-$ZnCl_2$, which is recognized as an intermediate case between a strong and fragile liquid. l-$ZnCl_2$ has a well-defined but not sharp FSDP in $S_{NN}(Q)$ owing to the contribution of corner-sharing $ZnCl_4$ tetrahedra, while edge sharing also occurs [52].

This behavior of the fragile glass former is very similar to that of l-$GeSe_2$, for which the FSDP in $S_{NN}(Q)$ is weak, and a considerable fraction of edge-sharing $GeSe_4$ tetrahedra contribute [53], as in glassy $GeSe_2$ [54]. We supeculate that the fragility of liquid increases with the contribution of edge-sharing tetrahedra, as discussed in Reference [55].

7 Conclusions

We have reported the recent development of the HEXTS and AXS instrumentation at SPring-8 together with the development of levitation techniques. HEXTS and AXS have become indispensable techniques for uncovering the atomistic structure in disordered materials. It is also stressed that the combination of HEXTS/AXS/EXAFS and the neutron scattering technique is the best approach for revealing short- and intermediate range ordering in disodered materials. Furthermore, we have reviewed recent research topics on glasses, high-temperature liquids, and amorphous materials involving advanced experiments and theories.

The use of coherent X-rays is one of the most important topics for next generation synchrotron radiation sources. Some pioneering studies have been reported on the investigation of aperiodic materials using X-ray cross-correlation analysis [56]. The results demonstrate the importance and benefit of using coherent X-rays. To promote the advanced science of disordered materials in future, it is desiable to use high-energy coherent X-rays in combination with advanced theory to unravel the "ordering" in disordered materials [57, 58], which is hidden in the pair correlations.

Acknowledgement: The synchrotron radiation experiment was carried out with the approval of the Japan Synchrotron Radiation Research Institute (JASRI) (Proposal Nos. 2010B1069, 2010B1144, 2011B1219, 2011B1220, 2011B1508, 2011B2001, 2011B2086, 2012A1213, 2012A1801, 2012A1837, 2012B1975, 2013A1049, 2013A1199, 2013A1897, 2013B1914, 2013B1915, 2015A1165, 2015A1480, and 2015A2056).

References

1. H. F. Poulsen, J. Neuefeind, H.-B. Neumann, J. R. Schneider, and M. D. Zeidler, J. Non-Cryst. Solids **188** (1995) 63.
2. Y. Waseda, *Anomalous X-ray Scattering for Materials Characterization*, Springer, Heidelberg (2002).

3. S. Hosokawa, Y. Wang, J.-F. Bérar, J. Greif, W.-C. Pilgrim, and K. Murase, Z. Phys. Chem. **216** (2002) 1219.
4. S. Hosokawa, I. Oh, M. Sakurai, W.-C. Pilgrim, N. Boudet, and J.-F. Bérar, Phys. Rev. B **84** (2011) 014201.
5. V. Petkov and S. D. Shastri, Phys. Rev. B **105** (2010) 165428.
6. V. Petkov, S. M. Selbach, M.-A. Einarsrud, T. Grande, and S. D. Shastri, Phys. Rev. Lett. **105** (2011) 185501.
7. S. Kohara, H. Tajiri, C. H. Song, K. Ohara, L. Temleitner, K. Sugimito, A. Fujiwara, L. Pusztai, T. Usuki, S. Hosokawa, Y. Benino, N. Kitamura, and K. Fukumi, J. Phys. Conf. Ser. **502** (2014) 012014.
8. S. Kohara, M. Itou, K. Suzuya, Y. Inamura, Y. Sakurai, Y. Ohishi, and M. Takata, J. Phys.-Condens. Mat. **19** (2007) 455214.
9. M. Isshiki, Y. Ohishi, S. Goto, K. Takeshita, and T. Ishikawa, Nucl. Instrum. Meth. A **467–468** (2001) 663.
10. O. Sakata, Y. Furukawa, S. Goto, T. Mochizuki, T. Uruga, K. Takeshita, H. Ohashi, T. Ohata, T. Matsushita, S. Takahashi, H. Tajiri, T. Ishikawa, N. Nakamura, M. Ito, K. Sumitani, T. Takahashi, T. Shimura, A. Saito, and M. Takahasi, Surf. Rev. Lett. **10** (2003) 543.
11. D. L. Price, *High-Temperature Levitated Materials*, Cambridge University Press, Cambridge (2010).
12. D. A. Winborne, P. C. Nordine, D. E. Rosner, and N. F. Marley, Metall. Trans. B **7B** (1976) 711.
13. W.-K. Rhim, S. K. Chang, D. Barber, K. F. Man, G. Gutt, A. Rulison, and R. E. Spjut, Rev. Sci. Instrum. **64** (1993) 2961.
14. T. Masaki, T. Ishikawa, P.-F. Paradis, S. Yoda, J. T. Okada, Y. Watanabe, S. Nanao, A. Ishikura, K. Higuchi, A. Mizuno, M. Watanabe, and S. Kohara, Rev. Sci. Instrum. **78** (2007) 026102.
15. J. K. R. Weber, C. A. Rey, J. Neuefeind, and C. J. Benmore, Rev. Sci. Instrum. **80** (2009) 083904.
16. C. J. Benmore and J. K. R. Weber, Phys. Rev. X **1** (2011) 011004.
17. W. H. Zachariasen, J. Am. Chem. Soc. **54** (1932) 3841.
18. D. T. Bowron, A. K. Soper, K. Jones, S. Ansell, S. Birch, J. Norris, L. Perrott, D. Riedel, N. J. Rhodes, S. R. Wakefield, A. Botti, M.-A. Ricci, F. Grazzi, and M. Zoppi, Rev. Sci. Instrum. **81** (2010) 033905.
19. H. Masai, Y. Takahashi, T. Fujiwara, S. Matsumoto, and T. Yoko, Appl. Phys. Express **3** (2010) 082102.
20. H. Masaki, R. Shirai, K. Yoshida, Y. Takahashi, R. Ihara, T. Fujiwara, Y. Tokuda, and T. Yoko, Chem. Lett. **42** (2013) 1305.
21. R. K. Brow, J. Non-Cryst. Solids **263&264** (2000) 1.
22. R. McGreevy and L. Pusztai, Mol. Simulat. **1** (1988) 359.
23. J. Akola, S. Kohara, K. Ohara, A. Fujiwara, Y. Watanabe, A. Masuno, T. Usuki, T. Kubo, A. Nakahira, K. Nitta, T. Uruga, J. K. R. Weber, and C. J. Benmore, P. Natl. Acad. Sci. USA **110** (2013) 10129.
24. P. K. Gupta and A. R. Cooper, J. Non-Cryst. Solids **123** (1990) 14.
25. S. Kohara, J. Akola, H. Morita, K. Suzuya, J. K. R. Weber, M. C. Wilding, and C. J. Benmore, P. Natl. Acad. Sci. USA **108** (2011) 14780.
26. C. A. Angell, Science **267** (1995) 1924.

27. S. W. Kim, T. Shimoyama, and H. Hosono, Science **333** (2011) 71.
28. M. Wuttig and N. Yamada, Nat. Mater. **6** (2007) 824.
29. K. Ohara, L. Temleitner, K. Sugimoto, S. Kohara, T. Matsunaga, L. Pusztai, M. Itou, H. Ohsumi, R. Kojima, N. Yamada, T. Usuki, A. Fujiwara, and M. Takata, Adv. Funct. Mater. **22** (2012) 2251.
30. D. A. Baker, M. A. Paesler, G. Lucovsky, S. C. Agarwal, and P. C. Taylor, Phys. Rev. Lett. **96** (2006) 255501.
31. J. Akola, R. O. Jones, S. Kohara, S. Kimura, K. Kobayashi, M. Takata, T. Matsunaga, R. Kojima, and N. Yamada, Phys. Rev. B **80** (2009) 020201R.
32. J. K. Olson, H. Li, and P. C. Taylor, J. Ovonic Res. **1** (2005) 1.
33. S. Caravati, M. Bernasconi, T. D. Kühne, M. Krack, and M. Parrinello, Appl. Phys. Lett. **91** (2007) 171906.
34. J. J. Kim, K. Kobayashi, E. Ikenaga, M. Kobata, S. Ueda, T. Matsunaga, K. Kifune, R. Kojima, and N. Yamada, Phys. Rev. B **76** (2007) 115124.
35. L. Guttman, J. Non-Cryst. Solids **116** (1990) 145.
36. J. Akola and R. O. Jones, J. Phys.-Condens. Mat. **20** (2008) 465103.
37. G. Bruns, P. Merkelbach, C. Schlockermann, M. Salinga, M. Wuttig, T. D. Happ, J. B. Philipp, and M. Kund, Appl. Phys. Lett. **95** 043108 (2009).
38. J. H. Coombs, A. P. J. M. Jongenelis, W. van Es-Spiekman, and B. A. J. Jacobs, J. Appl. Phys. **78** (1995) 4918.
39. L. B. Skinner, A. C. Barnes, P. S. Salmon, L. Hennet, H. E. Fischer, C. J. Benmore, S. Kohara, J. K. R. Weber, A. Bytchkov, M. C. Wilding, J. B. Parise, T. O. Farmer, I. Pozdnyakova, S. K. Tumber, and K. Ohara, Phys. Rev. B **87** (2013) 024201.
40. L. B. Skinner, C. J. Benmore, J. K. R. Weber, J. Du, J. Neuefeind, S. K. Tumber, and J. B. Parise, Phys. Rev. Lett. **112** (2014) 157801.
41. S. Kohara, J. Akola, L. Patrikeev, M. Ropo, K. Ohara, M. Itou, A. Fujiwara, J. Yahiro, J. T. Okada, T. Ishikawa, A. Mizuno, A. Masuno, Y. Watanabe, and T. Usuki, Nat. Commun. **5** (2014) 5892.
42. L. B. Skinner, C. J. Benmore, J. K. R. Weber, M. A. Williamson, A. Tamalonis, A. Hebden, T. Wiencek, O. L. G. Alderman, M. Guthrie, L. Leibowitz, and J. B. Parise, Science **346** (2014) 984.
43. T. E. Faber and J. M. Ziman, Philos. Mag. **11** (1965) 153.
44. A. Takada, P. Richet, C. R. A. Catlow, and G. D. Price, J. Non-Cryst. Solids **345&346** (2004) 224.
45. R. D. Shannon and C. T. Prewitt, Acta Crystallogr. B **25** (1969) 925.
46. A. B. Bhatia and D. E. Thornton, Phys. Rev. B **4** (1971) 3004.
47. P. S. Salmon, R. A. Martin, P. E. Mason, and G. J. Cuello, Nature **435** (2005) 75.
48. W. Tang, E. Sanville, and G. Henkelman, J. Phys.-Condens. Mat. **21** (2009) 084204.
49. Q. Mei, C. J. Benmore, S. Sen, R. Sharma, and J. Yargar, Phys. Rev. B **78** (2008) 144204.
50. A. C. Wright, Phys. Chem. Glasses **49** (2008) 103.
51. D. L. Price, A. J. G. Ellison, M.-L. Saboungi, R.-Z. Hu, T. Egami, and W. S. Howells, Phys. Rev. B **55** (1997) 11249.
52. A. Zeidler, P. S. Salmon, R. A. Martin, T. Usuki, P. E. Mason, G. J. Cuello, S. Kohara, and H. E. Fischer, Phys. Rev. B **82** (2010) 104208.
53. P. S. Salmon, J. Non-Cryst. Solids **353** (2007) 2959.
54. I. Petri, P. S. Salmon, and H. E. Fischer, Phys. Rev. Lett. **84** (2000) 2413.

55. M. Wilson and P. S. Salmon, Phys. Rev. Lett. **103** (2009) 157801.
56. P. Wochner, C. Gutt, T. Autenrieth, T. Demmer, V. Bugaev, A. Díaz Ortiz, A. Duri, F. Zontone, G. Grübel, and H. Dosch, P. Natl. Acad. Sci. USA **106** (2009) 11511.
57. P. S. Salmon, Nat. Mater. **1** (2002) 87.
58. D. A. Keen and A. L. Goodwin, Nature **521** (2015) 303.